Research Square

Preprints are preliminary reports that have not undergone peer review.
They should not be considered conclusive, used to inform clinical practice,
or referenced by the media as validated information.

Current-Induced Vortex Dynamics in a Superconducting extended Nano-bridge: A Time-Dependent Ginzburg-Landau Approach

D. C. Camargo-Barajas
Universidad Nacional de Colombia
C. Valenzuela-Rodriguez
Universidad Nacional de Colombia
J. Barba-Ortega
Universidad Nacional de Colombia
C. A. Aguirre
caguirret@udistrital.edu.co
Universidad Distrital Francisco José de Caldas
C. A. Gómez-Vasco
Universidad Distrital Francisco José de Caldas

Research Article

Keywords: Superconductivity, Vortex state, Meso-sample, Abrikosov, Shapiro jumps, Kinematic vortex

Posted Date: August 14th, 2026

DOI: https://doi.org/10.21203/rs.3.rs-10636900/v1

License: This work is licensed under a Creative Commons Attribution 4.0 International License.
Read Full License

Additional Declarations: No competing interests reported.

Current-Induced Vortex Dynamics in a Superconducting extended Nano-bridge: A Time-Dependent Ginzburg-Landau Approach.

D. C. Camargo-Barajas, C. Valenzuela-Rodriguez, and J. Barba-Ortega
Departamento de Física, Universidad Nacional de Colombia, Bogotá, Colombia.

C. A. Aguirre and C. A. Gómez-Vasco
Departamento de Física, Universidad Distrital Francisco José de Caldas, Bogotá, Colombia.

(Dated: August 8, 2026)

In this work, we study a superconducting nano/bridge in the presence of an external magnetic field and laterally applied currents. A specific number of symmetrically spaced subdivisions has been introduced into the system (we will call them legs). With this, we compute the main electronic variables, such as the magnetization and the scalar potential, as functions of the applied external current for a fixed external magnetic field and as functions of the external magnetic fields for a fixed external current. Due to this variation, we will study, in separate sections, the behavior of Abrikosov and kinematic vortices; for a second variation, we study the different values of the first Shapiro step that are observed. Subsequently, we present the Cooper pair density and the total current in the superconducting sample, together with the phase of the superconductor condensate. These results allow us to understand the influence of vortices in the mesoscale sample and how these subdivisions increase or decrease the first critical currents and the number of vortices in the sample, establishing a valid proposal for organized control of the fluxoids in the superconducting meso-sample.

Key words: Superconductivity; Vortex state; Meso-sample; Abrikosov; Shapiro jumps; Kinematic vortex.

I. INTRODUCTION

Over the last few decades, we have witnessed the widespread application of technology in various aspects of daily life, pushing it to limits that were unthinkable before this revolution [1–3]. Thus, in recent years, there have been significant leaps in data processing and Big Data storage [4], culminating in the implementation of various quantum computers that have been used to solve problems that are inconceivable for conventional computers, due to the complexity or the time required for their solution [5, 6]. However, the innovation on which much of our technology is based relies on materials called semiconductors [1–4, 7]. While these have enabled this revolution, they present two major shortcomings [8]. The first is the significant ohmic loss (Joule effect) they exhibit [8–10]. Second, because processing power is highly dependent on temperature, considerable energy is required to keep these new servers at low temperatures, enabling guaranteed higher processing speeds [8, 11]. This has limited the performance of these computers to date, and it is important to emphasize that this is a fundamental problem with the types of materials currently used; this includes the new quantum computers, because superconducting circuits have not yet been developed for this new technological implementation [13, 14].

Given the above, it has become necessary to change the focus to the materials used in new supercomputers; for this, the materials called to be implemented as a fundamental solution are the so-called superconductors [14–16]. These, in conventional terms, are divided into two large groups: (i) Type I and (ii) Type II [17, 18]. The first ones present a complete shielding of the externally applied magnetic field (Meissner-Oschenfeld Effect) and the conduction of the electric current (superconducting current) without Ohmic losses [1–3, 5, 8, 13, 19], at a certain critical temperature; the latter, although they allow the magnetic field to enter the sample, do so quantized and in coexistence with the normal state (called the Shuvnikov state)[21, 22]. This allows the movement and stabilization of vortices (topological defects), which are largely responsible for the material's different magnetic responses [21–23]. By defining the material's inherent interactions, these vortices can enable the coordinated movement of the supercurrent during the transition of electronic elements from semiconductor to superconducting versions, which exhibit higher efficiencies [24], shorter computation times [25], and lower energy losses [26]. Therefore, special emphasis has been placed on the study and manipulation of the vortex state through significant variations in geometries (conventional and unconventional) and different symmetries in meso-systems [23–27]. Finally, over the last 5 years, attempts have been made to design systems similar to conventional electronic systems, but in a superconducting version [27, 28]. Excellent efficiencies have been achieved in different diodes. Special emphasis has been placed on periodic systems, in which organized and periodic distributions of the order parameter can be generated, which can be used for the inflection of superconducting potentials, for structured storage of these superconducting nano/structures, taking into account the proximity interactions in these mesos/tructures; in

fact, some functional systems have been designed, based on a superconducting meso-bridge [29–31].

In the present work, we study the main electronic variables, the most important being the magnetization and the scalar potential in a superconducting meso-bridge, with different periodic additions of sub-bridges, which allow the symmetric division of the superconducting sample into subsections, allowing the control of the also periodic location of the Cooper pair density, generating a particularly interesting interaction of the super/current (See Fig. 1), in addition to applied external current, which can be manipulated to improve the performance in the organized processing of the Qubits, if considered as a superconducting chip. Next, we study the phase behavior of the superconducting condensate, which allows us to study the distribution of topological defects within the superconducting sample, together with the distribution of the total current in the sample. Finally, we emphasize the fact that the distance between these periodic sections does not exhibit a proximity interaction, because it is greater than the coherence length.

This paper is organized as follows. Section I describes the theoretical framework, including the time-dependent Ginzburg–Landau equations used in our analysis. Section II shows the main results of our numerical simulations, including voltage-current characteristics, first critical current, diode efficiency, and vortex nucleation varying κ or magnetic fields. Finally, we summarize our conclusions and outline future directions in Section III.

II. THEORY AND MODEL

We studied a real two-dimensional superconducting meso-bridge under a fixed external magnetic field ($\mathbf{H} = \mathbf{H}_z$) applied in the $\hat{z}$ direction. The geometry of our superconducting meso-sample is illustrated in Fig. (1). The interface between the lateral region and the vacuum is denoted by $\partial\Omega_i$, $i = 1, 2$ (sections where the external current enters). The dimension of the numerical sample is A×B. With this in mind, an external transport current ($\mathbf{J}$) -in $-\hat{x}$-direction- is applied to the superconducting meso-sample on the lateral side of the geometry. In this work, we employ the Generalized Time-Dependent Ginzburg-Landau Theory (**TDGL**), formulated under the dirty limit and expressed in dimensionless units, as described in Refs. [1, 2, 5, 10, 16, 21–26, 30, 31].

$$\frac{1}{\sqrt{1+\Gamma^2|\psi|^2}}\left[\frac{\partial\psi}{\partial t}+\frac{\Gamma^2}{2}\frac{\partial|\psi|^2}{\partial t}+\Phi\psi\right] = (i\boldsymbol{\nabla}+\mathbf{A})^2\psi+\psi(1-|\psi|^2), \tag{1}$$

for the potential vector:

$$\frac{\partial\mathbf{A}}{\partial t} = \mathbf{J}-\kappa^2(\boldsymbol{\nabla}\times\boldsymbol{\nabla}\times\mathbf{A}), \tag{2}$$

where:

$$\mathbf{J} = \mathrm{Re}\left[\bar{\psi}(-i\boldsymbol{\nabla}-\mathbf{A})\psi\right]-\boldsymbol{\nabla}\Phi, \tag{3}$$

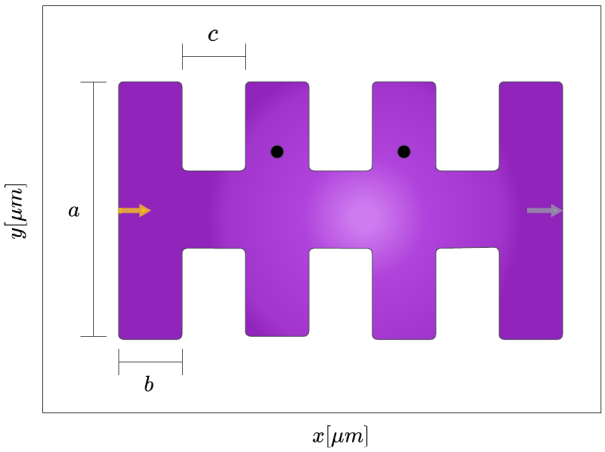


FIG. 1: Geometrical parameters defining the superconducting layout. The total height is denoted by a, while b and c correspond to the widths of the lower and upper constrictions, respectively. All dimensions are given in units of the coherence length $\xi(0)$. The system consists of a superconducting multi-constriction structure with periodic modulations along the transport direction. The yellow arrow indicates the incoming current, while the gray arrow represents the outgoing current. The black dots denote the positions where the scalar potential difference is computed.

and κ characterize the type of superconductor by relating the spatial variation of the order parameter ψ to the penetration of the magnetic field into the sample. In **GL** theory, κ is a dimensionless quantity defined as the ratio between the magnetic penetration depth and the coherence length of the superconductor[32–35]. This parameter determines whether a material is classified as type I or type II: for $\kappa < 1/\sqrt{2}$ the superconductor is type I, while for $\kappa > 1/\sqrt{2}$ it is type II. The higher values of κ correspond to a softer vortex lattice, thus facilitating vortex penetration at lower values of $\mathbf{J}$. In conjunction with the continuity equation, which also adopted the Coulomb gauge $\nabla\cdot\mathbf{A} = 0$ and Maxwell's first law, the expression for the scalar potential (Φ) is obtained as a Poisson time-dependent equation, which is given by:

$$\boldsymbol{\nabla}^2\Phi = \frac{\partial\rho}{\partial t} = -\nabla\cdot\mathbf{J}. \tag{4}$$

The Eqs. (1)-(4) are solved in a self-consistent approach and the Neumann boundary conditions for the potential/external current are $\hat{\boldsymbol{n}}\cdot\nabla\boldsymbol{\Phi} = -\boldsymbol{J}$ in sections with external current ($\partial\Omega_i$, $i = 1, 2$) and $\hat{\boldsymbol{n}}\cdot\nabla\boldsymbol{\Phi} = 0$ in the other sections, with $\hat{\boldsymbol{n}}$ being a surface normal vector. In

addition, $\boldsymbol{J}$ corresponds to the total superconducting current density (Meissner plus external/transport). In the quasi-steady regime, $\partial_t \rho \simeq 0$, so that Laplace's equation ($\nabla^2 \Phi = 0$) holds in the bulk, with solvability requiring that the net injected current equals the extracted one. Because a pure Neumann problem determines Φ only up to an additive constant, we fix the reference by enforcing, e.g., $\langle \Phi \rangle_{\partial\Omega_2} = 0$. The instantaneous voltage is then computed as the difference of surface-averaged potentials at the electrodes (leads)

$$V(t) = \langle \Phi \rangle_{\partial\Omega_1} - \langle \Phi \rangle_{\partial\Omega_2}, \qquad \langle \Phi \rangle_S = \frac{1}{|S|} \int_S \Phi \, dS, \quad (5)$$

where, S denotes the leads surface—i.e., a subset of the boundary $\partial\Omega$—over which the potential is averaged. The voltage follows from time-averaging $V(t)$ over the stationary window. Furthermore, in Eqs. (1), (2), and (3), dimensionless units were introduced as follows: the order parameter ψ is in units of $\psi_\infty = \sqrt{-\alpha/\beta}$ (the order parameter at the Meissner-Oschenfeld state), where α and β are two phenomenological constants; $\boldsymbol{H}_1$ is the first critical field (Meissner-Oschenfeld field); lengths are in units of the coherence length ξ; time is in units of the Ginzburg-Landau characteristic time $t_{GL} = \pi\hbar/(8K_B T_c)$; fields are in units of $\boldsymbol{H}_{c2}$, where $\boldsymbol{H}_{c2}$ is the bulk second critical field; the vector potential $\boldsymbol{A}$ is in units of $\xi \boldsymbol{H}_{c2}$; $\kappa = \lambda/\xi$ is the GLP, which describes the type of superconductor as a function of the spatial variation of the order parameter ψ and the penetration of the magnetic field into the sample and $\Gamma = 10$.Therefore, a dual mesh composed of Voronoi cells is intrinsically associated with the Delaunay triangulation. This duality enables the approximation of spatial derivatives by evaluating fluxes across the edges of the Voronoi cells. The resulting discretized equations employed in the method are given by [36–39]:

$$\frac{u(\psi_i^{n+1} e^{(i\mu_i^n \Delta t^n)} - \psi_i^n)}{\Delta t^n \sqrt{1+\gamma^2|\psi_i^n|^2}} + \frac{u\gamma^2 \left(|\psi_i^{n+1}|^2 - |\psi_i^n|^2\right)\psi_i^n}{2\Delta t^n \sqrt{1+\gamma^2|\psi_i^n|^2}} = \left(\epsilon_i - |\psi_i^n|^2\right)\psi_i^n + \frac{1}{a_i} \sum_{j\in\mathcal{N}(i)} \frac{U_{ij}^n \psi_j^n - \psi_i^n}{e_{ij}} s_{ij}, \quad (6)$$

and

$$\sum_{j\in\mathcal{N}(i)} \frac{\mu_j^n - \mu_i^n}{e_{ij}} s_{ij} = \sum_{j\in\mathcal{N}(i)} \mathrm{Im}\left\{ (\psi_i^n)^* \frac{U_{ij}^n \psi_j^n - \psi_i^n}{e_{ij}} \right\} |s_{ij}| - \sum_{j\in\mathcal{N}(i)} \frac{A_{ij}^n - A_{ij}^{n-1}}{\Delta t^n} |s_{ij}|. \quad (7)$$

For numerical calculations, we use the mesh size $\delta x = \delta y = \delta z = 0.1$, the constant values: $\eta = 5.79$, $\beta = 1.0$, $\zeta = 0.50$, $\kappa = 2.0$ and $\nu = 0.03$ [10, 13, 16, 19]. For tolerance in convergence of the order parameter ψ, we employ $\epsilon = 1.0^{-9}$, and the errors are of order $O(\Delta x)^2$ for space and time. For boundary conditions of the order parameter, we employ Robin's boundary condition $\mathbf{n} \cdot (i\boldsymbol{\nabla} + \mathbf{A})\psi = -i\psi/b$, with $\mathbf{n}$ being a surface normal vector and b, the de-Gennes extrapolation parameter and we have taken $b \to \infty$ in the lateral contacts and $b = 0$ in the rest of the sample. Finally, as shown in Fig. 1, the dimensions of the external numerical mesh are $A = 30\xi$, $B = 15\xi$ and $C = 1\xi$. Here, s_{ij} represents the stiffness matrix. In particular, **pyTDGL** incorporates an adaptive time-stepping algorithm that adjusts the time increment Δt^n according to the characteristic timescale of the system dynamics. This "nanobridge" geometries were constructed with `shapely`, initially defining the rectangular bars and bridges that were then unified into a single polygon. This polygon was converted into a **tdgl.Polygon** object and resampled to obtain smooth contours suitable for mesh generation [40, 41]. The applied field is prescribed by means of an external vector potential, whereas the current is injected through terminals defined on the outer legs. With that, we proceed with the main results of our superconducting sample.

III. NUMERICAL RESULTS

First, we present the magnetization, Cooper-pair density, and phase for the system under consideration (see Fig. 1(a)) for varying numbers of periodic subdivisions of the mesoscopic sample. Thus, in Fig. 2, we present the magnetization as a function of the external applied magnetic field, for different amounts of the periodic defects in the superconducting sample (legs), where we observe that in all the variations, they are initially in the Meissner-Oschenfeld state, after which, the slope in the magnetization changes and the vortices enter, and we observe that these first critical fields are different and decrease as we have a greater amount of periodic defects, this is because the inclusion of these defects affect the energy barrier at the borders, generating a decrease in it, allowing the vortices to enter more easily, after which, the system transitions to the normal state. However, due to the symmetry of the sample, we expect the vortices to position themselves in equilibrium at the center of the sample—where there is a greater amount of material—and to stabilize through their mutual interaction.

We now present the Cooper-pair density $|\psi|^2$ and the phase of the superconducting condensate (see Fig. 3) for the configuration featuring two larger side sections, under varying applied magnetic fields. We observe that at lower magnetic field values (Fig. 3(a)), two vortices are located near the central section of the sample; as the magnetic field increases, a greater number of vortices enter this central section. Due to their repulsive interaction, they lower the energy barrier in this area, causing it to transition to the normal state more rapidly than the more distant sections. Finally, the phase reveals the number of vortices present in the sample for the

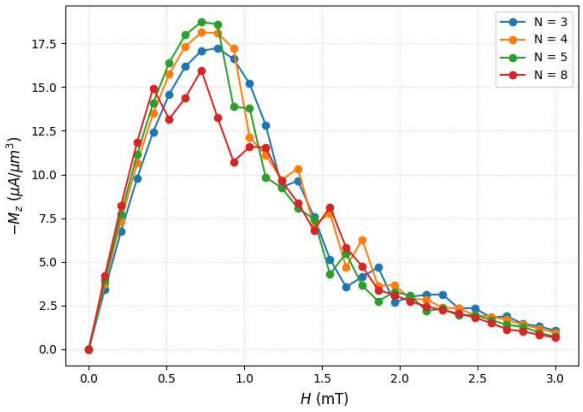
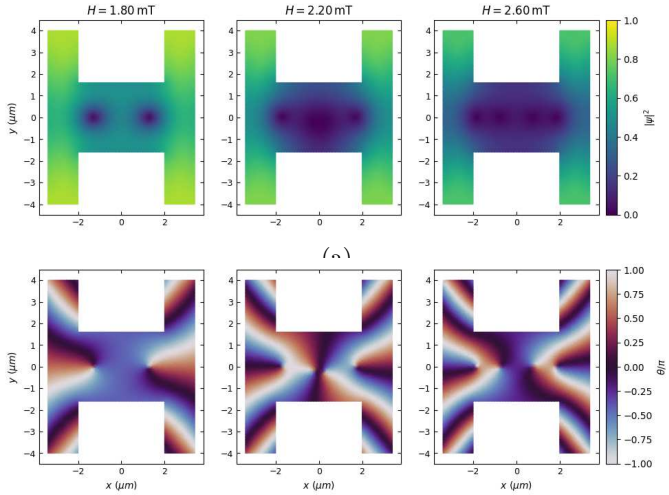


FIG. 2: Magnetization, as a function of the applied external magnetic field H, for the different number of legs and external current $\mathbf{J} = 0$.

specific field values analyzed, This study was conducted in the absence of external currents in order to compare the behavior with the inclusion of currents.



(b)

FIG. 3: Cooper-pair density $|\psi|^2$ (a) and phase ϕ showing vortex nucleation for increasing magnetic field, and magnetization (c), for the two-leg H geometry.

With this, we present in Fig. 4(a) the density of Cooper pairs for the superconducting system, in the presence of 3 symmetric divisions in the superconducting sample, for different values of the external magnetic field, but in the absence of external currents $\mathbf{J} = 0.0$. The initial observation is important: the vortices are located in the central position of the sample, at equidistant distances from each other, due to the interaction between the borders and between them. We observe that they are positioned in the superconducting sample, where there is greater symmetry, ignoring the fact that, in general, they are the positions with the

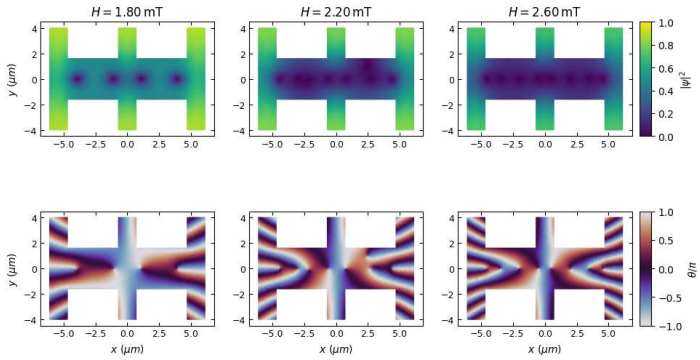


FIG. 4: Cooper pair density ($|\psi|^2$) and phase (ϕ) for three particular cases for a fixed number of periodic subdivisions of the superconducting meso-sample, for three values of the external magnetic field (a) $H = 1.80$mT, (b) $H = 2.20$mT, and (c) $H = 2.60$mT, all cases considered in the absence of external current.

greatest amount of material and that, as the value of the magnetic field increases, the number of vortices increases. Locating itself in the position that minimizes the energy, which in this case is the Gibbs free energy, are the central positions, so the transition to the normal state quickly follows the holding. Together, we present the phase ($\psi = |\psi|e^{i\phi}$), where we observe the behavior of the phase of the superconducting condensate.

With this, in Fig. 5(a), we present the density of Cooper pairs, for different values of the magnetic field in conjunction with different amounts of periodic defects, where it is clearly observed that due to the intrinsic size of the defects, in these sections the vortices do not enter, due to the high energy barrier, while in the central sections, the vortices are grouped periodically, causing this section to transition more quickly to the state normal. Now, observe the distribution of the vortices in the central sections, which allows establishing potentials between the vortices, which cause them to be in fixed positions of the sample, and due to the effect of repulsion with the first neighbors, they are forced to limit their movement, with only a certain very slight vibration being possible away from this equilibrium position.

Finally, in Fig. 6(a-h) we present the phase of the superconducting condensate, for the same values of the external magnetic field and the same amount of periodic defects in the mesosample. We observe that the field in the phase of the superconducting condensate coincides with the number of vortices inside and that, according to the amount of change in the phase, for the larger values of the applied external magnetic field, the vortices come together more, reaching a giant vortex near the center of the sample. Finally, as expected, within the defects (legs), there is no change in phase,

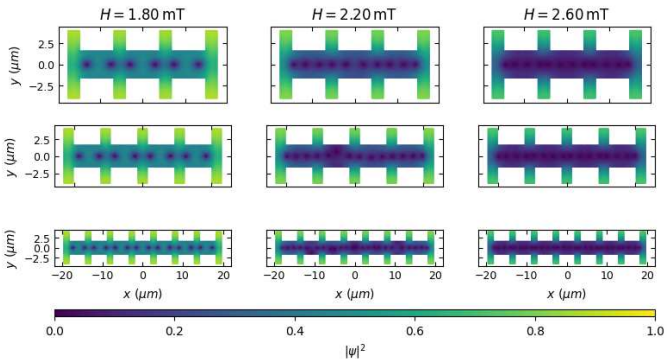


FIG. 5: Cooper pair density ($|\psi|^2$) for three particular cases of a fixed number of periodic subdivisions of the superconducting meso-sample, for three values of the external magnetic field (a) $H = 1.80$mT (b) $H = 2.20$mT and (c) $H = 2.60$mT, all cases considered in the absence of external current.

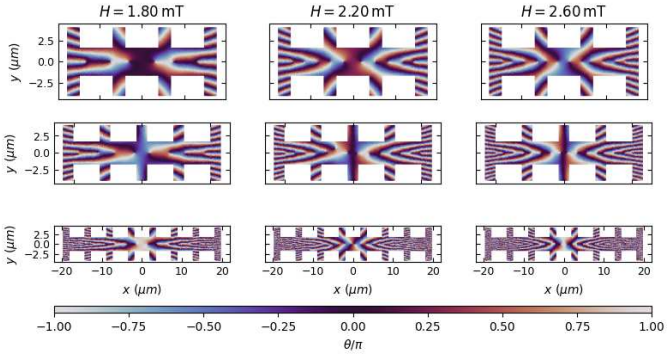


FIG. 6: Phase ϕ for H-shaped geometries with 4, and 8 legs at different magnetic fields.

indicating the absence of vortices (in the normal state).

This concludes the study of the state of vortices in the meso/superconducting system, in the absence of external currents, which only allows the existence of Abrikosov-type vortices. And more importantly, the fundamental fact of the existence and organization of these vortices as a function of the number of sample divisions and the applied external fields. Therefore, we present the kinematic vortices in the superconducting sample, arising from the field in the superconducting condensate phase induced by external currents in the absence of an applied magnetic field. These vortices form vortex-antivortex pairs that enter through the boundaries of the superconducting sample and move along the points of greatest symmetry, eventually annihilating at the system's maximum symmetry point. Thus, we initially calculate the scalar potential (voltage). In Fig. 7, we present this behavior of the scalar potential as a function of the applied external current and for different numbers of periodic systems (legs) of the superconducting meso-sample. As a result, we observe a change in the slope for certain currents; these changes are called Shapiro jumps. We observe that as the number of legs increases, these jumps occur at higher values of the applied current, indicating faster movement of the kinematic vortices and interaction between these lines, where the creation/annihilation of these pairs occurs. This also indicates a very rapid increase in the system's energy barrier near the boundary and, in these particular cases, a nonlinear addition of the total supercurrent in the sample. After this, the classical linear behavior is obtained, whose slope describes the resistive states in the superconducting sample.

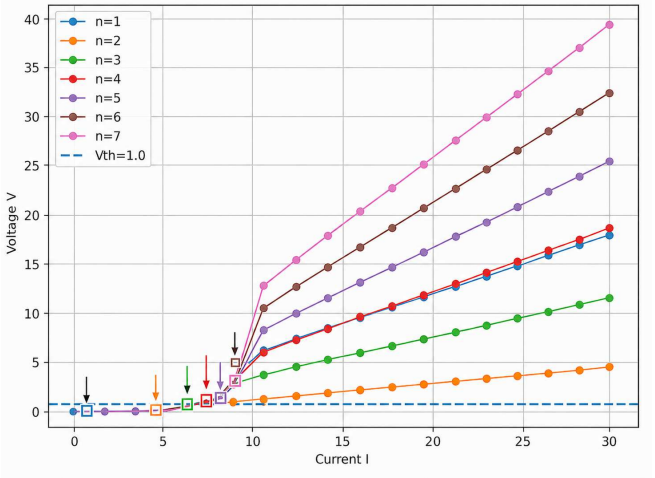


FIG. 7: Current–voltage characteristics for multi-leg devices (n = 1–7) showing the onset of the dynamical regime.

Now, in Fig. 8, we present the total current distribution in the superconducting sample—comprising both the superconducting current and the applied current. We clearly observe that, due to the periodic defects in the sample, the current streamlines exhibit oscillations around these defects; the resulting reduction in circulation leads to a periodic lowering of the barriers at these defect sites. Additionally, it is important to note the magnitude of the supercurrent at the center of the sample, where the maxima do not lie exactly along the same line parallel to the y-axis. This suggests that the difficulty of the current entering the periodic sections drastically affects vortex mobility, driving the vortices toward the center of the sample and—albeit with low probability—causing them to enter these sections.

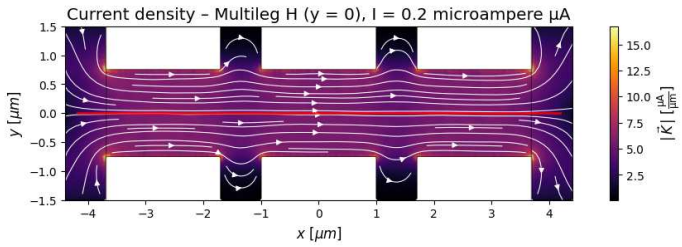


FIG. 8: Distribution of superconducting current for the case $J \neq 0$ and $H = 0$, for a five-leg geometry. The applied current corresponds to the dynamic critical current, with $I_{\text{source}} = +9\,\mu\text{A}$ and $I_{\text{drain}} = -9\,\mu\text{A}$.

To determine the appropriate dynamical regime for vortex nucleation, current–voltage (I–V) curves were first computed through a coarse current sweep, followed by a refined sampling around the onset of the resistive state. The dynamic critical current was defined as:

$$I_c^{\text{dyn}} = \arg\max_I \left(\frac{dV}{dI} \right) \tag{8}$$

The differential resistance was evaluated numerically using finite differences. Currents slightly above this threshold, typically in the range (1.03-1.10) I_c^{dyn}, were then selected to probe the kinematic vortex regime, where time-dependent phase-slip processes dominate the dynamics [26, 27, 30, 31]. For each selected current, vortices and anti-vortices were detected directly from the complex order parameter $\psi = |\psi| e^{i\theta}$ by computing the discrete winding number of the phase field over the triangular elements of the mesh. The phase $\theta = \arg(\psi)$ was evaluated at the mesh nodes, and for each triangle (a, b, c) the wrapped phase differences were computed in the principal branch $(-\pi, \pi]$. The local winding number was then obtained as:

$$w = \frac{1}{2\pi} \left(\Delta\theta_{ab} + \Delta\theta_{bc} + \Delta\theta_{ca} \right). \tag{9}$$

Triangles with $w = +1$ were classified as vortices, while $w = -1$ identified anti/vortices. To ensure robustness, only elements with sufficiently suppressed amplitude $|\psi|$ were retained, reflecting the fact that topological defects necessarily occur at points where the order parameter vanishes [8–11, 13, 14, 14–16]. Since multiple adjacent elements may correspond to a single physical core, detected candidates were grouped using a distance-based clustering procedure, yielding one effective center per vortex or anti/vortex. Finally, to distinguish bulk kinematic vortices from spurious defects induced by strong current injection near the electrodes, each detected center was classified according to its distance from the contact regions. Vortices located within a prescribed neighborhood of the terminals were labeled as `CONTACT`, while those sufficiently far from the boundaries were labeled as `BULK`. This separation is crucial in current-driven simulations, where boundary-induced suppression of superconductivity can otherwise bias the vortex count and obscure the intrinsic dynamical behavior of the system.

Vortex counting was carried out by identifying local zeros of $|\psi|^2$ and verifying phase singularities around each point. For each candidate, a small closed contour C was constructed, and the phase circulation was evaluated numerically by linearly interpolating the phase over the mesh triangles. The integral was discretized as a sum of angular differences corrected by 2π jumps, so that phase changes were projected onto the interval $(-\pi, \pi]$. Since this procedure relies directly on the local structure of the phase field, it is instructive first to examine the spatial distribution of θ. The phase is extracted from the complex order parameter $\psi = |\psi| e^{i\theta}$ as $\theta = \arg(\psi)$, consistently with the logarithmic representation $\ln \psi = \ln |\psi| + i\theta$. As shown in Fig. 9, the phase develops strong spatial gradients across the central bridge, together with localized distortions that signal the presence of topological singularities. These features provide the input for the winding number analysis described above.

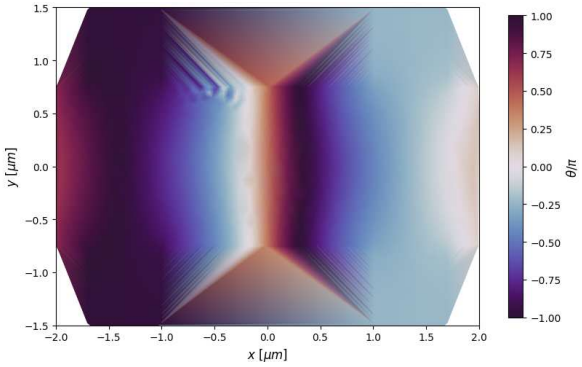


FIG. 9: Zoom of the superconducting phase distribution (θ/π) in the central region for the $n_{\text{legs}} = 5$ configuration under applied current. The phase gradients reflect the imposed current and exhibit localized distortions that anticipate the formation of vortex–anti/vortex pairs.

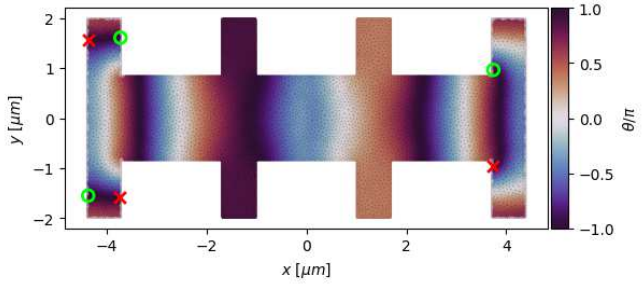


FIG. 10: Automatic detection and counting of vortices and anti/vortices using the winding number method in a multi-leg H-shaped superconducting geometry under applied current.

In Fig. 10, the spatial distribution of the vortex phase is shown for $n_{\text{legs}} = 4$. Topological singularities are identified via the winding number computed on the numerical mesh, where green circles denote vortices (+1) and red crosses anti/vortices (−1). Rather than relying exclusively on local minima of $|\psi|^2$, this identification is based on the quantized phase circulation, providing a direct characterization of the topological nature of the defects. The system is evaluated near the dynamic critical regime ($I \approx I_c$), where vortex–anti/vortex pairs emerge and contribute to dissipative transport, revealing their dependence on both geometry and applied current. From a physical perspective, the spatial distribution of the detected defects reflects the interplay between current-driven dynamics and the energy landscape imposed by the sample geometry.

In the absence of geometric perturbations, one might expect vortex–anti/vortex pairs to nucleate more symmetrically, for instance near the central region where phase gradients are strongest. However, it is well established that in mesoscopic superconductors the nucleation and motion of kinematic vortices are highly sensitive to current inhomogeneities and boundary conditions, which can significantly lower the energy barrier for vortex entry at specific locations. In particular, sharp edges, corners, and variations in width lead to current crowding, thereby creating preferred nucleation sites that are not necessarily aligned with geometrical centers. Although the global current is applied from left to right, the current-density distribution reveals a pronounced vertical redistribution, with streamlines bending and concentrating toward the outer corners of the lateral branches as is shown in 8. These regions act as effective edge hot spots, where the local current density is enhanced and the superconducting order parameter is more easily suppressed, favoring vortex entry. Consequently, the emergence of vortex–anti/vortex pairs near the extremities of the legs, rather than at the nominal phase origin, should be understood as a geometry-induced effect, where mesoscale boundary features govern the localization of topological defects and ultimately control the dissipative dynamics of the system.

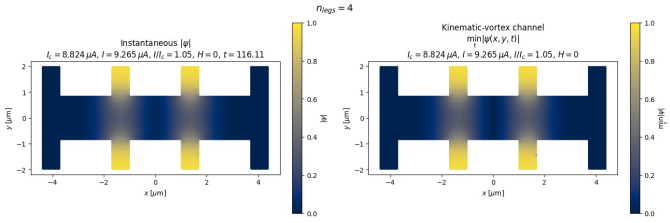


FIG. 11: Kinematic vortices for the meso-system under study, at specific values of the applied external current.

Finally, in Fig. 11, we present the Cooper-pair density for the mesoscopic system, including external currents, for specific values of the applied current. We observe channels forming near the defects—where the system remains superconducting while coexisting with a normal state—which allows for the observation of periodic normal/superconducting regions along the sample. This generates periodic potentials due to the potential barriers in the superconducting sections, potentially enabling control of this potential via the external current.

IV. CONCLUSIONS

In this work, we studied multi-bar superconducting nano/bridge geometries within the time-dependent Ginzburg–Landau framework, considering both magnetic-field-driven and current-driven regimes. The simulations show that the number of lateral legs strongly modifies the electromagnetic response of the system, affecting magnetization, current distribution, phase structure, and the onset of dissipative behavior. For the case $H \neq 0$ and $J = 0$, the results show that increasing the number of legs enlarges the number of effective regions where Abrikosov vortices can be accommodated, leading to distinct vortex distributions and changes in the magnetization curves as a function of the applied field. For the case $J \neq 0$ and $H = 0$, the I–V characteristics allowed us to estimate a dynamic critical current for each geometry, providing a reference scale for the onset of the resistive regime. Additionally, the spatial analysis of the order parameter, phase, and superconducting current reveals that the device geometry governs where dissipation first develops. In particular, the winding-number method confirmed the emergence of vortex–anti/vortex excitations near the dynamic regime. It showed that their location is strongly influenced by current crowding at edges and lateral branches. Altogether, these results demonstrate that multi-bar geometry is not a secondary detail, but a controlling factor in the vortex dynamics and transport properties of the nano/bridge. Finally, it is important to highlight that the inclusion of these multi-bars, combined with external current control, generates periodic patterns alternating between the normal and superconducting states; this creates a periodic energy barrier that allows for the control of kinematic vortices and, potentially, Abrikosov vortices. As future work, we will examine complementary geometries to determine more systematically under which conditions vortex–anti/vortex pairs nucleate, and how their formation depends on symmetry, confinement, and current distribution.

V. ACKNOWLEDGMENTS

C. Aguirre acknowledges S. Aguirre and M. Aguirre for useful discussions. C. Aguirre thanks the CNPq grant number process: 174045/2023-9 for financial support.

VI. REFERENCES

[1] L. Z. Deng, Z. Wu, T. Bontke, T. Habamahoro, D. Schulze, M. Gooch, T. W. Kuo, R. Fujikawa and C. W. Chu. From high-temperature superconductivity to room-temperature superconductivity: From ambient to high pressure; from very high pressure to ambient again!?, IOP Conf. Ser.: Mater. Sci. Eng. **1302** (2023).

[2] J. Bekaert, A. Aperis, B. Partoens, P. M. Oppeneer, and M. V. Milošević, Advanced first-principles theory of superconductivity including both lattice vibrations and spin fluctuations: The case of FeB_4, Phys. Rev. B **97**, 014503 (2018).

[3] J. Barba-Ortega, E. Sardella, J. A. Aguiar, Temperature-dependent vortex matter in a superconducting mesoscopic circular sector, Physica C, **470** 1964 (2010).

[4] V. Moshchalkov, M. Menghini, T. Nishio, Q. H. Chen, A. V. Silhanek, V. H. Dao, L. F. Chibotaru, N. D. Zhigadlo, and J. Karpinski, Type-1.5 Superconductivity, Phys. Rev. Lett. **410**, 117001 (2009).

[5] L. R. Cadorim, A. R. de C. Romaguera, I. G. de Oliveira, R. R. Gomes, M. M. Doria, and E. Sardella, Intermediate type-I superconductors in the mesoscopic scale, Phys. Rev. B **103**, 014504 (2021).

[6] M. Nadeem, M. S. Fuhrer, and X. Wang, The superconducting diode effect, Nat. Rev. Phys. **5**, 558 (2023).

[7] C. A. Aguirre, P. Díaz, D. Laroze, A. S. Mosquera Polo and J. Barba-Ortega, Vortex state in a 3D superconducting mesoscopic wedge, Physica C **213**, 193 (1993).

[8] Ž. L. Jelić, M. V. Milošević and A. V. Silhanek, Velocimetry of superconducting vortices based on stroboscopic resonances, Scientific. Reports. **6**, 35687 (2016).

[9] S. Banerjee and M. S. Scheurer, Altermagnetic superconducting diode effect, Phys. Rev. B **110**, 024503 (2024).

[10] A. Gutfreund, H. Matsuki, V. Plastovets, A. Noah, L. Gorzawski, N. Fridman, G. Yang, A. Buzdin, O. Millo, J. W. A. Robinson and Y. Anahory, Direct observation of a superconducting vortex diode, Nature Communications. **14**, 1630 (2023).

[11] M. Castellani, O. Medeiros, A. Buzzi, A. Foster, M. Colangelo and K. K. Berggren, A superconducting full-wave bridge rectifier, Nat Electron. (2025).

[12] T. Golod and V. M. Krasnov, Demonstration of a superconducting diode-with- memory, operational at zero magnetic field with switchable nonreciprocity, Nat Commun. **13**, 3658 (2022).

[13] G. R. Berdiyorov, M. V. Milošević, and F. M. Peeters, Vortex configurations and critical parameters in superconducting thin films containing antidot arrays: Nonlinear Ginzburg-Landau theory, Phys. Rev. B **74**, 174512 (2006).

[14] M. V. Milošević and R. Geurts, The Ginzburg–Landau theory in application, Physica C, **470**, 19, 791-795, (2010).

[15] M. V. Milošević and R. Geurts, Vortex-vortex interaction in bulk superconductors: Ginzburg-Landau theory, Phys. Rev. B **83**, 05451 (2011).

[16] Y. Wang, M. Li, C. Pei, L. Gao, K. Bu, D. Wang, X. Liu, L. Yan, J. Qu, Critical current density and vortex phase diagram in the superconductor, Phys. Rev. B **106**, 054506 (2022).

[17] S. Kozlov, J. Lesueur, D. Roditchev, et al, Dynamic metastable vortex states in interacting vortex lines, Commun Phys **7**, 183 (2024).

[18] R. Wördenweber, P. Dymashevski, V. R. Misko, Guided vortex motion in superconductors with asymmetric pinning landscapes, Phys. Rev. B **69**, 184504 (2004).

[19] C. Reichhardt, C. J. Olson Reichhardt, Vortex ratchets and diode effects in superconductors with periodic pinning arrays, Phys. Rev. B **78**, 224511 (2008).

[20] G. Carapella; V. Granata; F. Russo; G. Costabile, Bistable Abrikosov vortex diode made of a Py–Nb ferromagnet-superconductor bilayer structure, Appl. Phys. Lett. **94**, 242504 (2009).

[21] Boris Chesca, Daniel John, Richard Pollett, Marat Gaifullin, Jonathan Cox, Christopher J. Mellor, and Sergey Savelev, Magnetic field tunable vortex diode made of $YBa_2Cu_3O_{7-\delta}$ Josephson junction asymmetrical arrays, Appl. Phys. Lett. **111**, 062602 (2017).

[22] T. Golod, A. Pagliero, and V. M. Krasnov, Two mechanisms of Josephson phase shift generation by an Abrikosov vortex, Phys. Rev. B **100**, 174511 (2019).

[23] Changlong Wang, Guojing Hu, Xiang Ma, Haige Tan, Junjie Wu, Yan Feng, Shasha Wang, Ruimin Li, Bo Zheng, James Jun He, and Bin Xiang Superconducting-diode effect induced by inversion-symmetry breaking in a stepped $NbSe_2$ nanoflake, Phys. Rev. Applied 22, 064017 (2024).

[24] W. Gillijns, A. V. Silhanek, V. V. Moshchalkov, Origin of reversed vortex ratchet motion, Phys. Rev. Lett. **99**, 24 (2007).

[25] F. Liu, Y. M. Itahashi, S. Aoki, Y. D. Ziquian, N. Ogawa, T. Ideue and Y. Iwasa, Superconducting diode effect under time-reversal symmetry, Science Advances, **10**, 31 (2024).

[26] S. Banerjee and M. S. Scheurer, Altermagnetic superconducting diode effect, Phys. Rev. B **110**, 024503 (2024).

[27] Y. Zhang, Y. Gu, P. Li, J. Hu and K. Jiang, General Theory of Josephson Diodes, Phys. Rev. X, **12**, 041013 (2022).

[28] P. B. Chakraborty, A. Sivakumar, P. K. et al, Josephson diode effect from Cooper pair momentum in a topological semimetal, Nat. Phys. **18**, 1228–1233 (2022).

[29] M. Davydova, S. Prembabu and L. Fu, Universal Josephson diode effect, Sci. Adv. **8**, 0309 (2022).

[30] Jorge Cayao, Naoto Nagaosa, and Yukio Tanaka, Enhancing the Josephson diode effect with Majorana bound states, Phys. Rev. B **109**, L081405 (2024).

[31] R.S. Souto, M. Leijnse, C. Schrade, Josephson diode effect in supercurrent interferometers, Phys. Rev. Lett. **129**, 267702 (2022).

[32] A. Costa, O. Kanehira, H. Matsueda, and J. Fabian, Unconventional Josephson supercurrent diode effect induced by chiral spin-orbit coupling, Phys. Rev. B **111**, L140506 (2025).

[33] F. Ando, Y. Miyasaka, T. Li, J. Ishizuka, T. Arakawa,

Y. Shiota, T. Moriyama, Y. Yanase and T. Ono, Observation of superconducting diode effect, Nat. Phys. **584**, 373 (2020).

[34] J. Hasan, D. Shaffer, M. Khodas and A. Levchenko, Superconducting diode efficiency from singlet-triplet mixing in disordered systems, Phys. Rev. B **111**, 174514 (2025).

[35] S. Qi, J. Ge, C. Ji, Y. Ai, G. Ma, Z. Wang, Z. Cui, Y. Liu, Z. Wang and J. Wang, High-temperature field-free superconducting diode effect in high-T_c cuprates, Nat. Commun. **16**, 531 (2025).

[36] Igor de M. Froldi, Hermann Freire, Efficiency of the superconducting diode effect of pair-density-wave states in two-dimensional d-wave altermagnets, Annals of Physics, **483**, 170273, (2025).

[37] X. Zeng, R. Zhang, G. Guo, Z. Gao, Q. Hu, H. Ji, F. Yang, X. Wang, B. Gao, N. F. Q. Yuan, B. Lv, X. Liu, H. Ding, Large superconducting diode effect driven by edge states in twisted iron-chalcogenide Josephson junctions, arXiv:2510.00595 [cond-mat.supr-con] (2025).

[38] D. Chakraborty, A. M. Black-Schaffer, Perfect Superconducting Diode Effect in Altermagnets, Phys. Rev. Lett. **135**, 026001, (2025).

[39] J. J. He, Y. Tanaka and N. Nagaosa, A phenomenological theory of superconductor diodes, New J. Phys. **24**, 053014, (2022).

[40] Ba. Pal, A. Chakraborty, P. K. Sivakumar, M. Davydova, A. K. Gopi, A. K. Pandeya, J. A. Krieger, Y. Zhang, M. Date, S. Ju, N. Yuan, N. B. M. Schröter, L. Fu and S. S. P. Parkin, Josephson diode effect from Cooper pair momentum in a topological semimetal, Nat Commun **15**, 8014 (2024).

[41] J. Jun He, Y. Tanaka and N. Nagaosa, A phenomenological theory of superconductor diodes, New J. Phys. **24** 053014 (2022).